Observations of sound-speed fluctuations in the Beaufort Sea from summer 2016 to summer 2017

Murat Kucukosmanoglu, John A. Colosi, Peter F. Worcester, Matthew A. Dzieciuch, and Daniel J. Torres

Citation: The Journal of the Acoustical Society of America **149**, 1536 (2021); doi: 10.1121/10.0003601
View online: https://doi.org/10.1121/10.0003601
View Table of Contents: https://asa.scitation.org/toc/jas/149/3
Published by the Acoustical Society of America

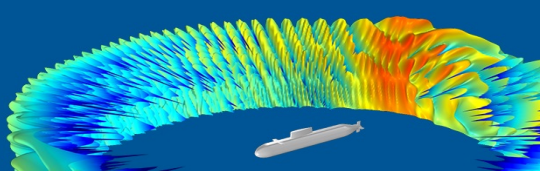

JASA ARTICLE

Observations of sound-speed fluctuations in the Beaufort Sea from summer 2016 to summer 2017[a)]

Murat Kucukosmanoglu,[1,b)] John A. Colosi,[2,c)] Peter F. Worcester,[3,d)] Matthew A. Dzieciuch,[3,e)] and Daniel J. Torres[4]

[1]*Department of Ocean Sciences, University of California, Santa Cruz, California 95060, USA*

[2]*Department of Oceanography, Naval Postgraduate School, Monterey, California 93943, USA*

[3]*Scripps Institution of Oceanography, University of California San Diego, La Jolla, California 92093, USA*

[4]*Department of Physical Oceanography, Woods Hole Oceanographic Institution, Woods Hole, Massachusetts 02543, USA*

ABSTRACT:

Due to seasonal ice cover, acoustics can provide a unique means for Arctic undersea communication, navigation, and remote sensing. This study seeks to quantify the annual cycle of the thermohaline structure in the Beaufort Sea and characterize acoustically relevant oceanographic processes such as eddies, internal waves, near-inertial waves (NIWs), and spice. The observations are from a seven-mooring, 150-km radius acoustic transceiver array equipped with oceanographic sensors that collected data in the Beaufort Sea from 2016 to 2017. Depth and time variations of the sound speed are analyzed using isopycnal displacements, allowing a separation of baroclinic processes and spice. Compared to lower latitudes, the overall sound speed variability is small with a maximum root mean square of 0.6 m/s. The largest source of variability is spice, most significant in the upper 100 m, followed by eddies and internal waves. The displacement spectrum in the internal wave band is time dependent and different from the Garrett-Munk (GM) spectrum. The internal wave energy varied with time averaging 5% of the GM spectrum. The spice sound-speed frequency spectrum has a form very different from the displacement spectrum, a result not seen at lower latitudes. Because sound speed variations are weak, observations of episodic energetic NIWs with horizontal currents up to 20 cm/s have potential acoustical consequences.

 https://doi.org/10.1121/10.0003601

(Received 11 July 2020; revised 2 December 2020; accepted 8 February 2021; published online 5 March 2021)

[Editor: Mohsen Badiey] Pages: 1536–1548

I. INTRODUCTION

The Arctic Ocean is of considerable interest in the context of its changing processes such as currents, thermohaline structure, and sea ice extent. Sea ice in the Arctic Ocean has dramatically declined in recent decades (Maslanik *et al.*, 2007; Stroeve *et al.*, 2012) with more notable decreases in September than in winter (Stroeve *et al.*, 2014). Significant variations in temperature (DiMaggio *et al.*, 2018) and freshwater content (Haine *et al.*, 2015) have also been observed. Using observations from the 2016–2017 Canada Basin Acoustic Propagation Experiment (CANAPE), this paper seeks to quantify the effects of these changes and important ocean processes, such as eddies, internal waves, internal tides, and temperature/salinity variability, along isopycnals (spice) on Arctic sound speed and current structure.

Mesoscale eddies induce large changes in the sound speed at lower latitudes (Worcester *et al.*, 1999). This is the case in the CANAPE observations to the extent that sub-inertial sound-speed fluctuations dominate the variability. Beaufort Sea eddies are mostly anticyclonic and can cover up to one-quarter of the ocean surface area (Carpenter and Timmermans, 2012; Zhao *et al.*, 2014). Most eddies exist in the upper ocean halocline and are observed to be strong below the mixed layer (Brannigan *et al.*, 2017). Because eddies are often generated in frontal regions, core and surrounding water masses differ. To the extent that there are instabilities, spicy water is formed from the comingling of the water masses giving rise to sound speed perturbations (Fine *et al.*, 2018). This is in addition to the sound speed changes that result from the doming of isopycnals, which are caused by the circulation of the eddy. The CANAPE observations are interesting in that the sub-inertial variations in the sound speed are dominated by spice rather than by displacement effects.

Internal tides can also produce large shallow and deep water sound speed anomalies that are important to sound propagation (Colosi *et al.*, 2012, 2013). Internal tides are generated by barotropic tidal flows interacting with the topography (Garrett and Kunze, 2007; Munk and Wunsch, 1998). They can be a source for the broadband internal wave field through spectral energy transfer by nonlinear wave-wave interaction (Bell, 1975; Levine *et al.*, 1987).

[a)]This paper is part of a special issue on Ocean Acoustics in the Changing Arctic.

[b)]Electronic mail: mkucukos@ucsc.edu, ORCID: 0000-0003-3611-7692.

[c)]Also at: Department of Ocean Sciences, University of California, Santa Cruz, CA 95060, USA, ORCID: 0000-0003-3817-8798.

[d)]ORCID: 0000-0001-8758-6849.

[e)]ORCID: 0000-0001-7926-7602.

https://doi.org/10.1121/10.0003601

Internal tides are relatively weak in many regions of the Arctic Ocean compared to other oceans (Lyard, 1997). In addition, they mainly do not exist at latitudes higher than 75.05°N at the M2 frequency (Levine *et al.*, 1987). In this work, the moorings were close to the M2 critical latitude, making internal tides indistinguishable from near-inertial waves (NIWs). There is a moderate peak in the displacement spectrum at twice the tidal frequency; however, this peak might be related to nonlinear internal tide generation processes. The acoustical consequences of this peak are unknown.

The broadband field of stochastic internal waves has been studied for decades in relation to sound propagation (Colosi, 2016; Flatté *et al.*, 1979). Internal wave energy levels in the Arctic are quite low, although recent studies have found that the internal wave energy level has risen because of increased momentum fluxes from the atmosphere as a consequence of the rapid decline in the sea ice extent in the Canada Basin (Dosser and Rainville, 2016; Rainville *et al.*, 2011). The CANAPE observations show a weak internal wave field with energies roughly 5% of the Garrett-Munk reference energy (Munk, 1981). Additionally, previous studies have found the Arctic internal wave energy level and spectral shape to be quite variable in time (Levine *et al.*, 1987). The CANAPE observations reinforce this notion of a nonstationary internal wave spectrum in which the spectral energy varies by a factor of 3 and the spectral shape changes markedly from slopes of −1.1 to −0.5.

A relatively new topic to sound propagation in the ocean is that of sound speed anomalies along isopycnals, generated by compensating temperature and salinity structure or spice (Colosi *et al.*, 2013; DiMaggio *et al.*, 2018; Dzieciuch *et al.*, 2004). The Arctic Ocean differs from ice-free oceans because the temperature near the freezing point has a minor effect on the density (Timmermans and Jayne, 2016). Therefore, a small salinity anomaly requires a large temperature anomaly to be density compensated, thereby giving rise to a large sound speed anomaly. In the CANAPE observations, spice is generally observed between the Arctic surface water (ASW) and the Pacific summer water (PSW) in which there is mixing between the warm and salty PSW and cold and less saline ASW. Changes in the temperature (T) and salinity (S) between these water masses result in sound speed variations up to several meters/second in the upper 100 m. Additionally, like the internal wave spectrum, the spice sound speed spectrum (energy and spectral shape) is found to be quite variable in time.

NIWs induce fluctuations in the horizontal current by driving water parcels mostly in horizontal circles with a relatively weaker vertical motion (Colosi, 2016). NIWs can originate from sea ice motion and winds at the surface in the Arctic Ocean (D'Asaro, 1985; Dosser and Rainville, 2016; Rigby, 1976) and typically generate currents of the order of tens of centimeters per second. These waves are of interest to Arctic acoustics because sound-speed fluctuations due to eddies and internal wave displacements are also of the order of several tens of centimeters per second. Previous studies have found the energy of NIWs to be 1 to 2 orders of magnitude weaker under the ice cover than in other oceans (Halle and Pinkel, 2003; Levine *et al.*, 1987; Morison *et al.*, 1985). NIW energy in the Arctic is significantly higher in summer when the sea ice is absent (Dosser *et al.*, 2014; McPhee, 2008; Rainville and Woodgate, 2009) despite weaker winds than in winter (Overland, 2009). A possible explanation is that thicker ice in winter, particularly for concentrations above 90%, may lead to a significant decrease in momentum transfer from the wind to the water column (Martini *et al.*, 2014). The CANAPE observations generally support these views, but episodic NIW events that are larger than most of the open water NIWs were observed under the ice.

The organization of the paper is as follows. Section II discusses the CANAPE observations of T, S, the current, and the methods of analysis. Frequency spectra of isopycnal displacements and spicy sound speed anomalies are described in Sec. III, together with the varying energy level as a function of depth. In Sec. IV, NIWs were analyzed to describe the spatial and temporal variability throughout the annual cycle. The paper finishes with the final summary and conclusions in Sec. V.

II. EXPERIMENT

The CANAPE experiment aims to assess the present ocean acoustic conditions in the Beaufort Sea with a focus on physical oceanographic processes that impact sound propagation on varying space and time scales up to the annual cycle. This effort was carried out between 26 August 2016 and 2 October 2017, using six acoustic transceiver moorings and one distributed vertical line array (DVLA) receiver mooring, each equipped with various oceanographic sensors such as temperature, conductivity, depth (CTD), temperature alone, acoustic Doppler current profilers (ADCP), and ice profiling sonars (IPS). In this work, the time-coordinate is identified in yeardays beginning with 1 January 2016, 1200 UTC as yearday 1.5. Figure 1 shows the overall experimental geometry and bathymetry, and it should be noted that the array straddles the latitude where the Coriolis frequency matches the M2 tidal frequency, an important consideration with regard to inertial waves and internal tides. Table I gives the locations and water depths for all 7 moorings.

A. CANAPE observations

Here, the oceanographic instrumentation on the seven CANAPE moorings used in this study are described. The DVLA was the main source of the data quantifying the variable thermohaline structure because it was equipped with a dense array of CTD instruments. Full water depth shipboard CTDs were also taken at each mooring during the deployment and recovery cruises. The DVLA CTD sensors provided the detailed salinity and temperature data required for separating internal waves and spice (Colosi *et al.*, 2012, 2013). This included 28 Sea-Bird MicroCats (SBE 37-SMP/SM), sampling every 5 min and spanning

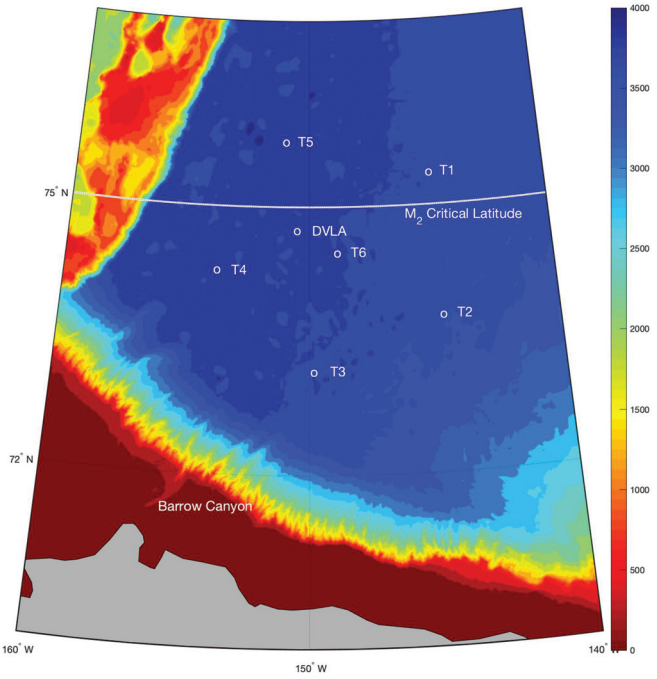

FIG. 1. The mooring geometry for CANAPE 2016, consisting of six acoustic transceivers (T1–T6) and a distributed vertical line array (DVLA) receiver located at the intersection of the T1–T4 and T3–T5 paths. The topography is from Sandwell/Smith (Becker *et al.*, 2009; Smith and Sandwell, 1997, 2014).

50–425-m depths with a typical separation of 13.5 m. The DVLA also had an upward-looking 75 kHz Teledyne RDI ADCP (Poway, CA) at a 613-m depth with a sample interval of 3 h and a range of approximately 300–400 m and a downward-looking 150 kHz Teledyne RDI ADCP at 625-m depth with a sample interval of 30 min and a range of approximately 100–200 m.

Both ADCPs had an 8-m bin size. The DVLA oceanographic instrumentation is listed in Table II. The DVLA and T1–T6 hydrophone modules (HMs) recorded temperature, respectively, at 20-min and 12-min intervals, and there were ten temperature sensors on each of the T-moorings that recorded at 10-s (SBE 56) and 5-s (RBRsolo T, Ottawa, Ontario, Canada) intervals. These temperature data were not used in the present analysis because there was no accompanying salinity data. Table III shows the oceanographic instrumentation on a "typical" T-mooring. Additionally, on the subsurface floats of the T1–T6 moorings, there were upward-looking 600 kHz Teledyne RDI ADCPs used to quantify the NIW variability and 420 kHz IPS to give ice thickness. All the moorings were moving with the currents (Colosi *et al.*, 2018) but were acoustically navigated by a long baseline system with 3–4 bottom transponders. This navigation is required to use the observed acoustic travel times for tomography and ocean model data assimilation. The navigation data reveal that the DVLA watch circle radius, primarily driven by tides and NIWs, was typically 50–100 m with vertical excursions of a few tens of meters. More dramatic mooring motion is seen when an eddy is present. These events lead to horizontal deflections of several hundreds of meters and vertical displacements ranging from roughly 50 to 100 m.

TABLE I. CANAPE mooring locations and water depths.

Mooring	Latitude (N)	Longitude (W)	Water depth (m)	Range to DVLA (km)
T1	75.3633°	145.0522°	3780	176.335
T2	73.7870°	144.8043°	3711	207.299
T3	73.1807°	149.9738°	3771	176.338
T4	74.3018°	153.9499°	3860	108.980
T5	75.7177°	151.1767°	3842	108.977
T6	74.5027°	149.0122°	3816	57.299
DVLA	74.7476°	150.6729°	3845	0

B. Thermohaline observations

Mean profiles of the temperature, salinity, sound speed, buoyancy frequency, potential density, and potential sound speed gradient obtained from shipboard and the DVLA moored CTD data between 16 September 2016 and 13 June 2017 are displayed in Fig. 2. Four distinct water masses can be identified. Starting from the top of the water column, ASW is cold and fresh, PSW is warmer and saltier than ASW, Pacific winter water (PWW) is colder and saltier than PSW, and, last, Atlantic water (AW) is warm and salty. In Fig. 2, the ASW from the CTD shows high temperatures near the surface due to summer solar heating.

The two temperature maxima at 86 m and 495 m are associated with PSW and AW, respectively, and the temperature minimum at 215-m depth is associated with PWW.

Two haloclines are present, a strong one in the ASW and a weaker one between the PWW and the AW. The ASW halocline gives rise to strong density stratification, leading to buoyancy frequencies up to 10 cycles per hour (cph). The effect of the deeper halocline is also seen with an increase in buoyancy frequency.

To illustrate the CTD observations, depth-time series of temperature, salinity, and sound speed anomalies are displayed in Fig. 3 (left), showing the variability observed in the upper 200 m during the passage of an eddy. The eddy is characterized by cold-fresh waters roughly between yearday 285 and 300 and warm-salty waters roughly between yearday 300 and 315. Sound speeds change abruptly across this transition, but the isopycnals deviate only slightly. There is also a great deal of sound speed structure in the upper 100 m that is attributable to spice. Anomalies below 200 m did not change significantly over the year, showing that the dominant sound speed variability is in the upper 100 m. The yearlong CANAPE thermohaline structure and variability are nicely summarized in a *T*/*S* diagram (Fig. 3, right), computed using the DVLA moored CTD data between 16 September 2016 and 13 June 2017. The isopycnal contours are practically vertical because near the freezing point, the density is strongly driven by the salinity rather than the temperature. The four different water masses previously discussed are indicated on the *T*/*S* diagram. Because of its low

https://doi.org/10.1121/10.0003601

TABLE II. CANAPE DVLA mooring oceanographic instrumentation placement with the average depth. The hydrophone module (HM) depths are not shown.

Depth (m)	Instrument	Time duration	Depth (m)	Instrument	Time duration
51.4	SBE 37-SMP[a]	11 September–1 October	254.4	SBE 37-SMP	11 September–8 July
64.9	SBE 37-SMP	11 September–1 October	267.1	SBE 37-SMP	11 September–11July
78.4	SBE 37-SMP	11 September–1 October	280.8	SBE 37-SMP	11 September–1 October
92.0	SBE 37-SMP	11 September–1 October	294.4	SBE 37-SMP	11 September–1 October
105.5	SBE 37-SMP	11 September–1 October	308.1	SBE 37-SMP	11 September–1 Oct
118.6	SBE 37-SMP	11 September–1 October	329.8	SBE 37-SMP	11 September–1 October
132.1	SBE 37-SMP	11 September–1 October	343.4	SBE 37-SMP	11 September–1 Oct
145.5	SBE 37-SMP	11 September–1 October	357.0	SBE 37-SMP	11 September–1 October
159.5	SBE 37-SMP	11 September–22 June	370.4	SBE 37-SMP	11 September–1 October
172.6	SBE 37-SMP	11 September–25 May	384.2	SBE 37-SMP	11 September–1 October
186.1	SBE 37-SMP	11 September–13 June	399.2	SBE 37-SMP	11 September–1 October
199.4	SBE 37-SMP	11 September–10 July	410.2	SBE 37-SM[a]	11 September–1 October
212.9	SBE 37-SMP	11 September–17 August	423.7	SBE 37-SM	11 September–1 October
226.4	SBE 37-SMP	11 September–14 June	613.0	75 kHz ADCP[b]	9 October–1 October
240.0	SBE 37-SMP	11 September–1 October	625.0	150 kHz ADCP[b]	11 September–1 October

[a]The primary instruments are Sea-Bird Electronics models SBE37-SM and SBE37-SMP (pumped) MicroCAT CTD instruments. The SBE instruments sampled the ocean at 30-s intervals. The pressure sensors are accurate to 0.1% of full range, and various models are rated from 200 to 1000 dbar. Therefore the depth errors are between 1 and 0.2 m. This has a minimal effect on the analysis.
[b]A 75 kHz ADCP was deployed in the upward-looking direction and a 150 kHz ADCP was deployed in the downward looking direction.

salinity, ASW shows up on the left-hand side of the diagram. The subsurface temperature maximum identifies PSW, whereas the subsurface temperature minimum identifies PWW. AW is seen to be warm and salty. But, most intriguing in the *T*/*S* diagram are the changes in variability from layer to layer. AW is the least variable with the points forming a thin line. ASW and PSW are the most variable with clouds of points occupying large regions of θ-S space. Points scattered along a density contour represent spice; that is, the temperature and salinity vary, but the density is constant (Dzieciuch *et al.*, 2004). These spicy variations are acoustically significant because compensating temperature and salinity anomalies (hot and salty/cold and fresh) reinforce the sound speed (Colosi, 2016).

TABLE III. CANAPE T-mooring oceanographic instrumentation placement with average depth (BPR, bottom pressure recorder).

Depth (m)	Instrument	Depth (m)	Instrument
40	IPS-5/600 kHz ADCP[a]	158	HM
44	SBE 37-SMP	167	HM
50	HM	176	HM
59	HM	180	T-sensor[b]
68	HM	200	T-sensor
77	HM	225	T-sensor
86	HM	250	T-sensor
95	HM	280	T-sensor
104	HM	325	T-sensor
113	HM	375	T-sensor
122	HM	430	T-sensor
131	HM	490	T-sensor
140	HM	570	T-sensor
149	HM	3763	BPR

[a]IPS-5 is a 420 kHz ASL Environmental Sciences (Victoria, British Columbia, Canada) ice profiling sonar. A 600 kHz ADCP was deployed in the upward-looking direction.
[b]Temperature sensors were a mixture of Sea-Bird SBE 56 and RBRsolo T.

Most importantly for this acoustical work is that the thermohaline structure gives rise to two sound channels called the surface duct and the Beaufort duct. The surface duct is formed mostly from the strong halocline, leading to a sound speed minimum at the surface in winter, but in Fig. 2, the effect of the warm summer surface layer is evident. The Beaufort duct is formed by the cold PWW between the warmer PSW and AW. Additionally, the Beaufort duct potential sound speed gradient is close to zero, implying that sound-speed fluctuations induced by vertical displacements (such as internal waves) will be small. Unlike the surface duct, the Beaufort duct trapped sound is of sufficiently high frequency and expected to have low losses because it is shielded from lossy surface interactions. This sound channel can be crudely characterized as having a minimum (or axial) sound speed c_a at a depth z_a and a maximum sound speed c_m, above and below the axis at depths z^+ and z^-. The modal cutoff f_c frequency (Hz) for this general duct is approximately

$$f_c = \left(\frac{c_a^3}{\delta c}\right)^{1/2} \frac{1}{\delta z} \frac{3}{4\sqrt{2}} (n - 1/2), \tag{1}$$

where $\delta c = c_m - c_a$, $\delta z = |z^+ - z^-|$, and n is the mode number (see the Appendix for details). Some of the parameters of Eq. (1) are plotted in Fig. 4. For the mean and standard deviations of the Beaufort duct parameters derived from Fig. 4, it is found that δz is 144 ± 10 m, δc is 2.2 ± 0.4 m/s, and c_a is 1442 ± 0.1 m/s. The axial sound speed is found to be quite stable in time except for a roughly 1 m/s change around yearday 270. Another noteworthy point of this display is that the upper and lower boundaries of the

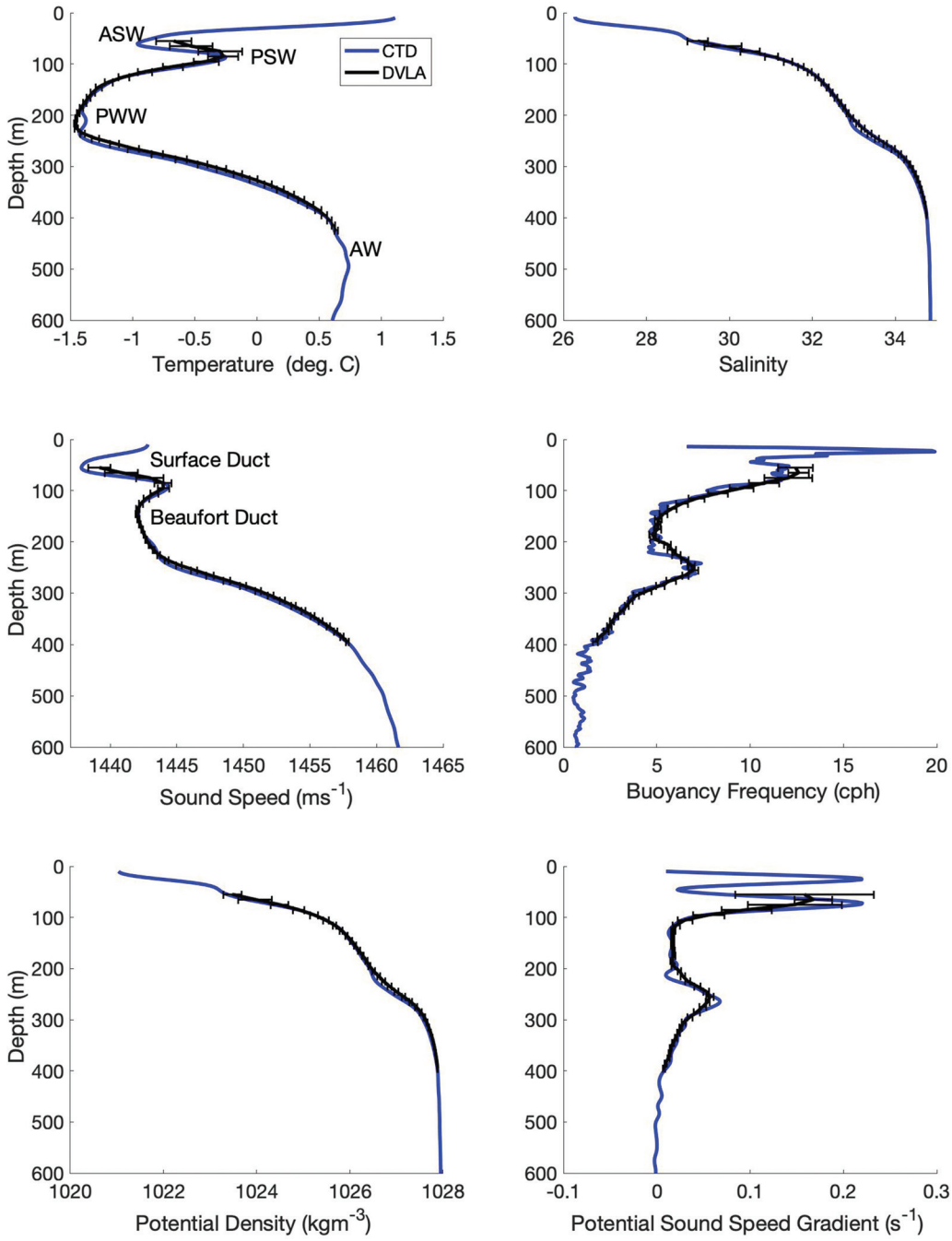

FIG. 2. Mean profiles of the temperature, salinity, sound speed, buoyancy frequency, potential density, and potential sound speed gradient in the upper 600 m. The root mean square (RMS) statistics derived from the DVLA are shown with black lines. Average profiles derived from CTD casts made near the DVLA during the deployment and recovery cruises are shown with blue lines.

Beaufort duct varied significantly between yearday 285 and 315 when the eddy with changing temperature and salinity, which is observed in Fig. 3. This eddy leads to significant changes in the modal cutoff frequencies by a factor of 2.

The Beaufort duct cutoff frequencies for modes 1–4 are 69 ± 12, 208 ± 36, 346 ± 60, and 484 ± 83 Hz, respectively. Mode 1 shows trapping at 100 Hz and higher frequencies, but at 50 Hz, the mode has spread out significantly (Fig. 5). Similar cases apply to other modes below their f_c's. Importantly for this experiment with acoustic frequencies between 200 and 300 Hz, it is expected that modes 1 and 2 are strongly trapped, mode 3 is marginally trapped, and modes 4 and above are not trapped.

C. Currents

The DVLA and T-mooring ADCP observations reveal energetic but isolated eddies and episodic strong NIWs (Fig. 6).

At the DVLA, a strong deep eddy is seen between 2016 yeardays 620 and 640, whereas the lower edges of shallower

https://doi.org/10.1121/10.0003601

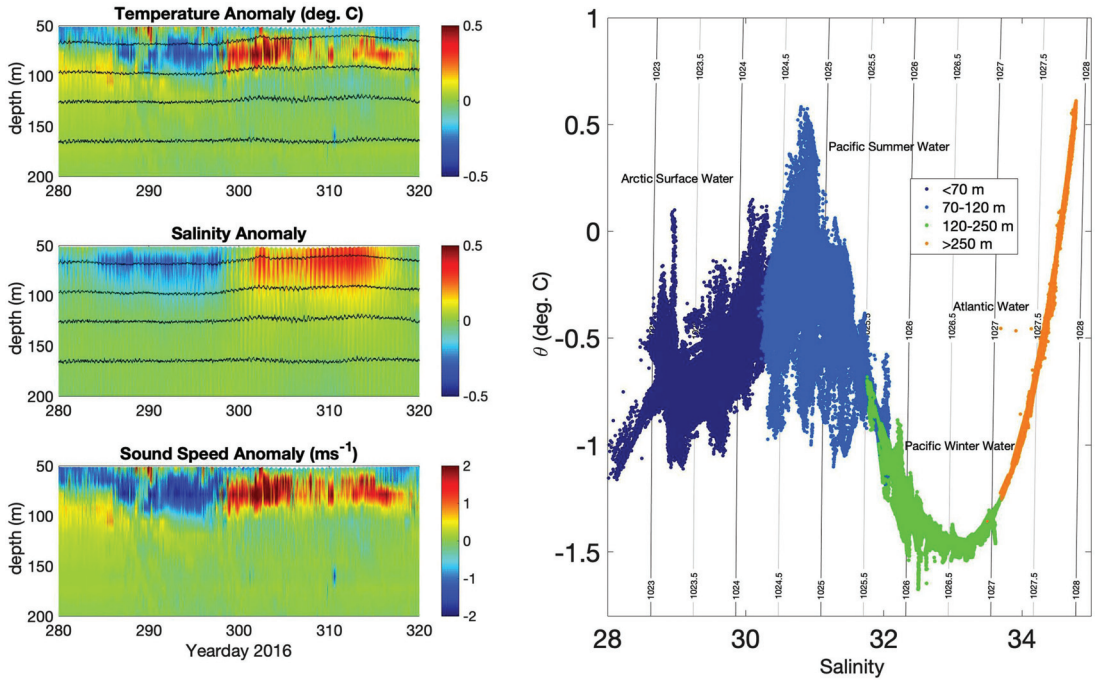

FIG. 3. The left panels shows the depth-time series of the temperature (top), salinity (middle), and sound speed anomalies (bottom) in the upper 200 m at the DVLA mooring between 6 October (yearday 280) and 15 November 2016 (yearday 320). A few isopycnals 1024, 1025.2, 1025.8, 1026.2 kg m^{-3} are overlaid in black. The right panel shows the potential temperature as a function of the salinity, illustrating the water mass properties at the DVLA mooring between 16 September 2016 and 13 June 2017. Black lines are the contours of the potential density. Colors represent depth regions (see the inset) as well as the labeled water masses.

eddies are seen between yeardays 590 and 620. These eddies are not seen simultaneously on the T6 ADCP because it is 57 km away, and typical eddy radii in this region are 4–16 km (Zhao *et al.*, 2014). Also, on the DVLA, downward propagation of the NIW packets is seen between yeardays 600 and 620. For the T6 mooring, energetic upper ocean NIWs exist between yeardays 580 and 640. They are seen to be more energetic after yearday 635. It will be shown that episodic NIWs have horizontal currents comparable to internal wave sound speed variations and, therefore, could be an important scatterer of acoustic energy. This issue will be taken up in later work.

D. Displacement and spice

Sound-speed fluctuations in the ocean can be driven by vertical displacements, which advect the strong vertical gradients, and accordingly there is

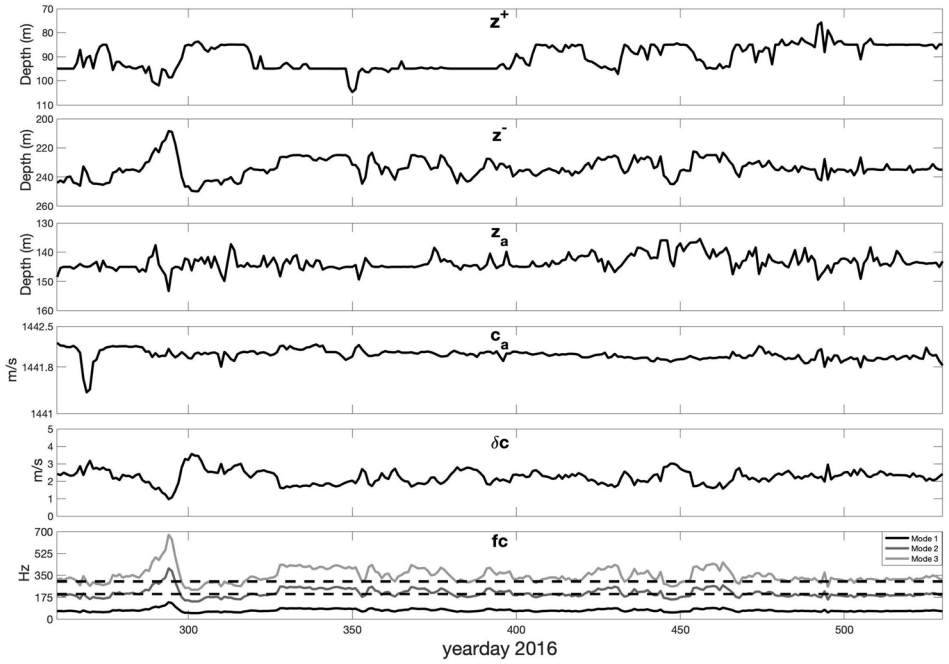

FIG. 4. The time series of the daily mean z^+, z^-, z_a, c_a, δc, and f_c in the Beaufort duct at the DVLA mooring between 16 September 2016 (yearday 260) and 13 June 2017 (yearday 530). The cutoff frequency, f_c, is computed using Eq. (1) for modes 1–3 in the bottom panel (black, dark gray, gray). The CANAPE low frequency band extending from approximately 200–300 Hz is indicated with dashed horizontal lines.

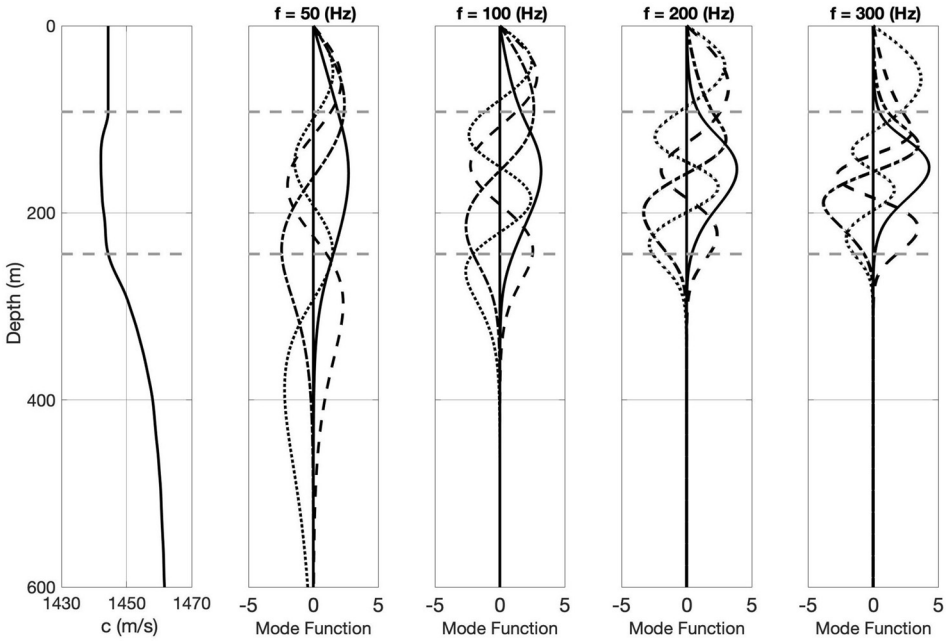

FIG. 5. Beaufort duct mode functions at 50, 100, 200, and 300 Hz are displayed for the mean sound speed profile in Fig. 2 after modification to remove the surface duct (solid line, mode 1; dashed-dotted line, mode 2; dashed line, mode 3; dotted line, mode 4). The surface duct is removed to focus on the Beaufort duct trapping behavior. Gray dashed lines indicate the upper and lower boundaries of the duct.

$$\delta c(r,t) = \left(\frac{dc(z)}{dz}\right)_p \zeta(r,t), \tag{2}$$

where the important factor is $(dc(z)/dz)_p$, the potential sound speed gradient, i.e., the total gradient minus the adiabatic gradient (Colosi, 2016). To quantify the space/time scales of displacements, the DVLA moored CTD observations were used, and standard isopycnal tracking techniques were applied (Colosi, 2016; Colosi *et al.*, 2013; DiMaggio *et al.*, 2018; Duda *et al.*, 2012). The potential density, $\sigma_0[z(t),t]$ (Talley, 2011), referenced to the surface (0 dbar), was computed as a function of the instrument depth $z(t)$ and time t. Next, the depths of 33 isopycnals were computed at approximately 10-m depth intervals using depth-

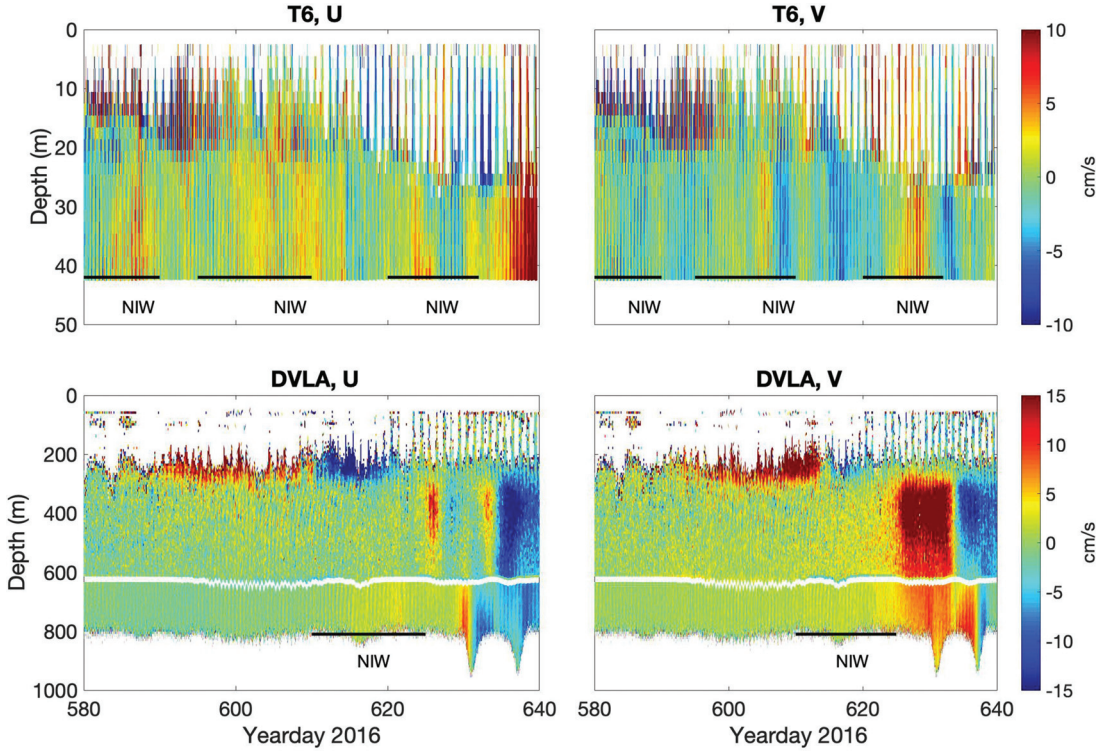

FIG. 6. The horizontal velocities as a function of depth and time, measured between 2 August (yearday 580) and 30 September 2017 (yearday 640). Upper graphs show the depth-time series of the u and v velocities at the T6 mooring, and lower graphs show the depth-time series of the u and v velocities at the DVLA mooring. The convention is u positive East and v positive North. Horizontal black lines indicate the approximate periods of the relatively strong NIWs.

https://doi.org/10.1121/10.0003601

linear interpolation. Figure 7 shows the entire record for 33 tracked isopycnals as well as an expanded region over 20 days. Many space and time scales are evident as is intermittency.

Eddies are evident between yeardays 285 and 315, and perhaps some eddy filaments or submesoscale structures are seen after yearday 500. Short time scale fluctuations (less than the inertial period) are evident in the records and clearly variable in time (more in the later period).

The isopycnal tracking method allows us to quantify temperature and salinity variations along isopycnals, refered to as spice (Fig. 8). For an isopycnal between the ASW and PSW, the T and S variations are large, leading to sound speed variations of several meters/second (Fig. 8, upper). For a deeper isopycnal between the PWW and AW, T, S, and sound speed variations are small. Figure 9 shows the time/depth structure of the spice. It is also seen that spice is strong in the upper 100 m and drops significantly in the Beaufort duct and the AW. This result is consistent with the T/S diagram.

III. SPECTRA

In this section, the frequency spectra of isopycnal displacements related to eddies, internal waves, and internal tides are quantified as are the spectra of spicy sound speed anomalies generated by T and S anomalies along isopycnals. The root mean square (RMS) variability of these quantities as a function of depth is also presented.

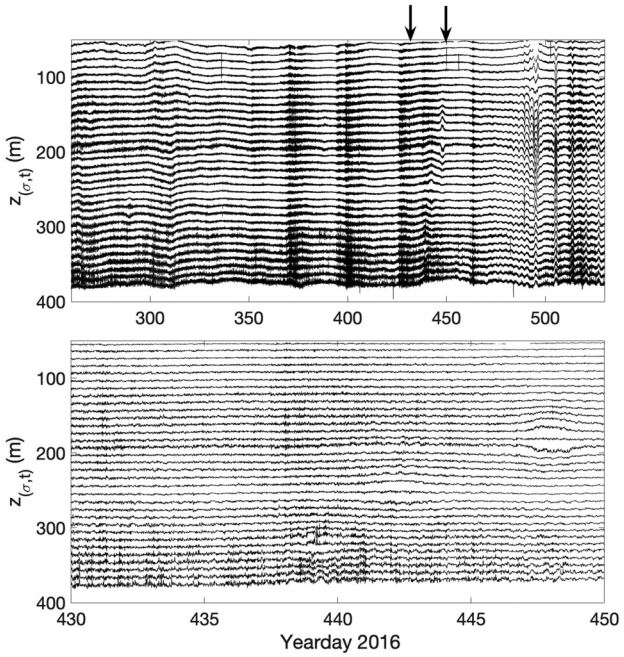

FIG. 7. Thirty-three tracked isopycnals as a function of depth and time at the DVLA mooring between 16 September 2016 (yearday 260) and 13 June 2017 (yearday 530) (upper) and between 5 March (yearday 430) and 25 March 2017 (yearday 450) (lower). After 13 June 2017, several of the Sea-Bird Electronics (Bellevue, WA) models SBE37-SM and SBE37-SMP below 150-m failed. Isopycnals are roughly separated by 10 m on average.

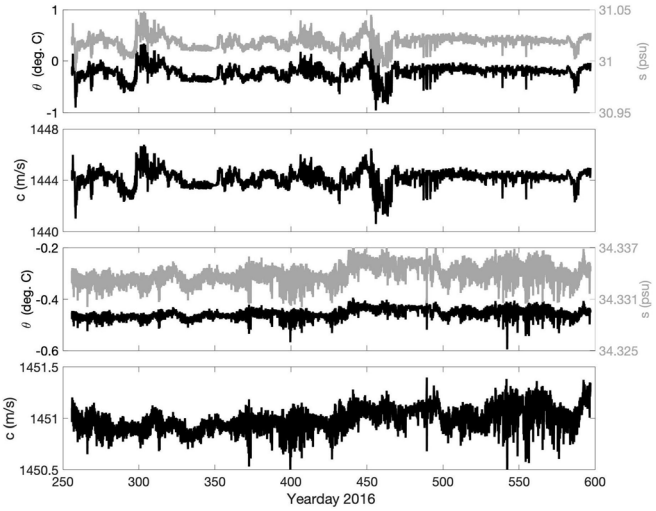

FIG. 8. Temporal fluctuations of the sound speed, potential temperature, and salinity along the isopycnal 1024.9 kg m^{-3} at 84.5-m depth (upper panels) and 1027.6 kg m^{-3} at 295.15-m depth (lower panels) between 16 September 2016 (yearday 260) and 19 August 2017 (yearday 597).

A. Internal waves, internal tides, and eddies

Figure 10 shows the frequency spectra of vertical displacements for two periods, 16 September 2016–28 February 2017 (upper) and 1 March–13 June 2017 (lower). During both periods, most of the energy in the internal wave band occurs in the near-inertial frequency region, from f - 1.1f, where f is Coriolis frequency. Energy decreases just below the inertial frequency, and then it rises again at lower frequencies due to eddy activity. Interestingly, in the internal wave band, there is a moderate peak at twice the tidal/

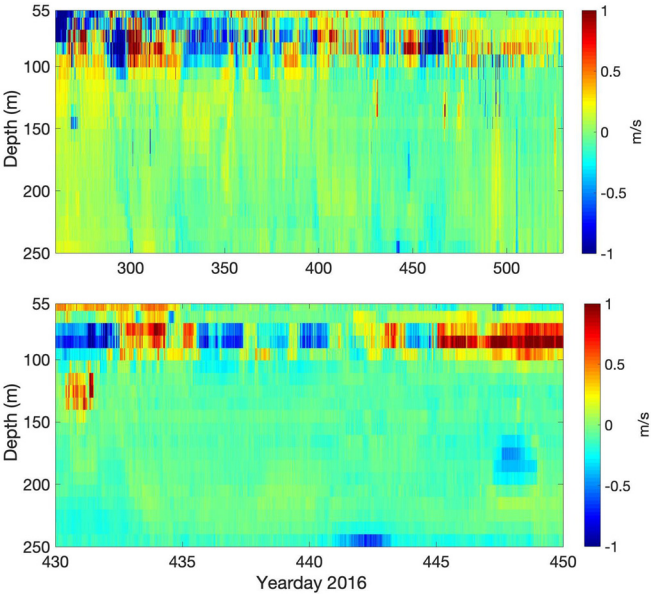

FIG. 9. The depth-time series of spicy sound speed anomalies measured at the DVLA mooring between 16 September 2016 (yearday 260) and 13 June 2017 (yearday 530; (upper) and between 5 March (yearday 430) and 25 March 2017 (yearday 450; lower).

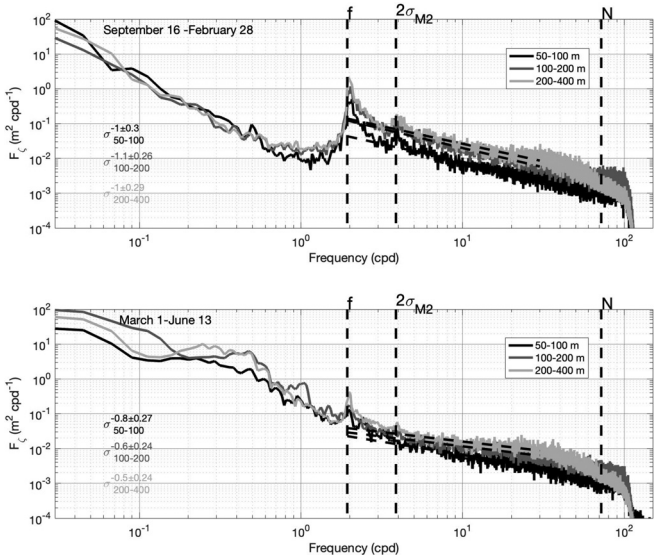

FIG. 10. Frequency spectra of isopyncal displacements for different depth bands (black, dark gray, gray) and different time periods (upper/lower). The Coriolis frequency, f, typical buoyancy frequency, N, and twice tidal frequency are indicated with dashed vertical lines. Power law fits (dashed lines) to the spectra between 2 and 30 cycles per day (cpd) are shown along with their power law exponents.

inertial frequency. The spectra show that a more energetic eddy field exists during the later part of the year.

The RMS variation of vertical displacements with depth is shown in Fig. 11. In the internal wave band, the observations are compared to Wentzel–Kramers–Brillouin (WKB) scaling, and the agreement is excellent for a reference internal wave displacement of 1.5 m. This can be compared to the Garret-Munk (GM) reference value of 7.3 m, which yields an average observed internal wave energy level that is roughly 5% of the GM value. The sub-inertial RMS displacements are seen to be roughly twice those in the internal

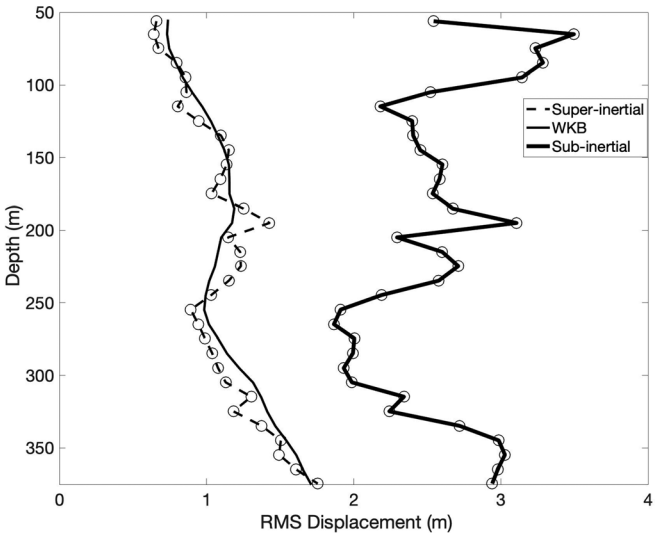

FIG. 11. The RMS displacement versus depth in the super-inertial (dashed line) and sub-inertial bands (bold solid line). The WKB equation, $\langle \zeta^2 \rangle = \zeta_0 \sqrt{N_0/N(z)}$, using a reference internal wave displacement $\zeta_0 = 1.5$ m, is plotted as a thinner solid line.

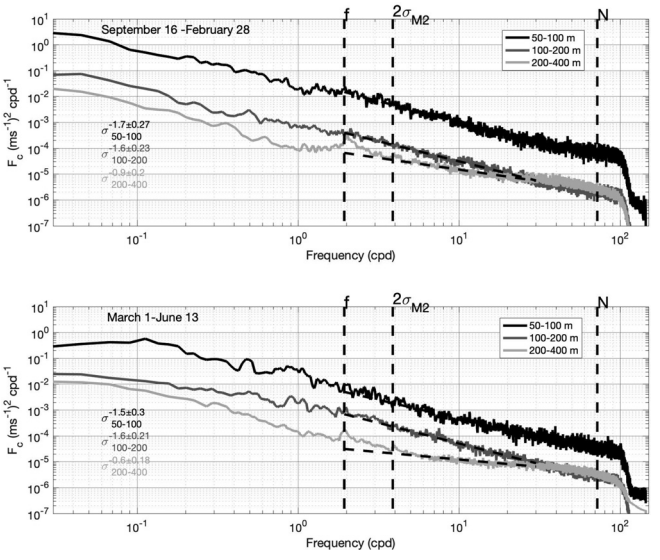

FIG. 12. Same as in Fig. 10 except for the spicy sound-speed fluctuations.

wave band, and this means that the sub-inertial variance accounts for 80% of the total.

B. Spice

Frequency spectra of spicy sound-speed fluctuations were computed for the same three-depth bands and time periods as for the isopycnal displacement spectra (Fig. 12). These spectra show a slight peak near the inertial frequency in the depth band 200–400 m but not in the depth bands 100–200 m and 50–100 m. The spice spectra are quite different from the displacement spectra and show less time dependence.

The RMS sound speed perturbations from spice and displacement are shown in Fig. 13 with contributions from the internal wave band, shown separately from the sub-inertial contributions. RMS displacement is converted to RMS sound speed using Eq. (2). Here, we see that spice dominates the upper ocean, whereas displacements and spice

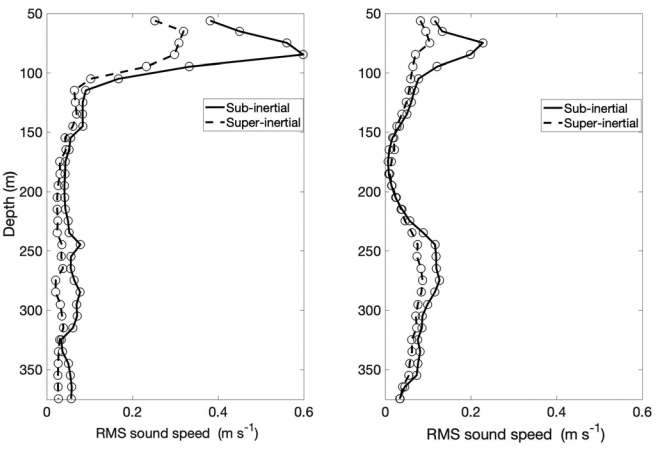

FIG. 13. The RMS sound speed for spice (left) and displacement (right) versus depth in the super-inertial (dashed line) and sub-inertial bands (solid line).

https://doi.org/10.1121/10.0003601

have more comparable contributions deeper down. The deep perturbations are weak indeed.

For the internal wave band, the spice is the more significant contributor to the sound speed variability in the upper 100 m. From 100 to 200 m, the spice and displacement contribution are comparable except for the axis of the Beaufort duct. However, the fluctuations due to vertical displacements induced by internal waves start to dominate below 200 m. For the sub-inertial band, spice is the larger contributor from the surface to a 100-m depth.

IV. NIWS

As seen in Fig. 13, the sound speed perturbations in the Canada Basin that result from internal waves and spice are generally small compared to those in other oceans. This implies that acoustic variability from these processes will be less significant than in other oceans. However, ADCP observations from this experiment suggest another source of acoustic variability, namely, upper ocean episodic, energetic NIW horizontal currents. Generally, small-scale inertial wave horizontal currents are neglected in fluctuation studies because sound-speed fluctuations dominate (i.e., $\delta c \gg u$), but NIW events where this condition breaks down were observed. There is well-developed literature on acoustics in moving media, particularly in the atmospheric acoustics setting (Ostashev and Wilson, 2015). Here, a sufficient view under the assumptions of low Mach number and small angle forward scattering is that an opposing/reinforcing current acts like a low/high sound speed zone.

The ADCP observations in this study are not ideal for quantifying NIW space and time scales. The 75 and 150 kHz ADCPs sample the depth region of approximately 300–800 m where NIWs are weak. This is because NIWs are generated at the surface by wind action. They propagate slowly down the water column, weaken as they propagate into lower stratification, and experience some loss (D'Asaro, 1985; Hebert and Moum, 1994). The upper ocean 600 kHz ADCPs are in a good water column location with strong stratification, but they have a limited depth sampling range (approximately 10–30 m) and are subject to large mooring motion effects. Be that as it may, the 600 kHz ADCPs on moorings T1–T6 provide a peek into the space and time scales of NIWs. The NIW analysis goes as follows. First, the observed hourly horizontal velocities (u,v) were corrected for the mooring motion. The T-moorings and DVLA were navigated using 3–4 bottom transponders that allow a solution for the (x,y,z) position of the hydrophone elements using acoustic travel times. A position was computed every hour, thus, permitting estimation of the horizontal mooring velocity at an adequate temporal resolution for NIW motions. The mooring-motion-corrected velocities were then high-pass filtered with a cutoff frequency of $^1/_4$ cpd giving the data used in the analysis (u_c,v_c) (Fig. 14). The NIWs are modeled as vertically propagating, anticyclonic (clockwise), circularly polarized currents that can be written in the form

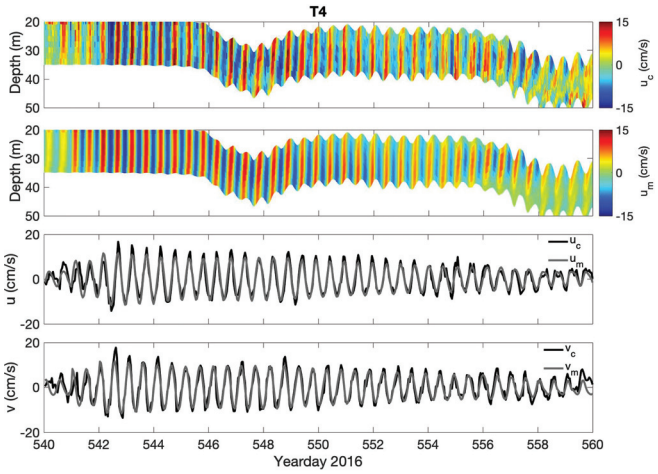

FIG. 14. Mooring T4's NIW currents showing u_c and u_m (upper panels) for the period 23 June (yearday 540) to 13 July 2017 (yearday 560). Depth-averaged currents u_c,v_c (black) and u_m,v_m (gray; lower panels). The convention is u positive East and v positive North.

$$u_m(z,t) = A(z)\sin(mz - ft), \tag{3}$$

$$v_m(z,t) = -A(z)\cos(mz - ft), \tag{4}$$

where $A(z)$ is a depth dependent current amplitude, m is a constant vertical wave number (no refraction), and $f = 2\Omega\sin(\text{latitude})$ is the inertial frequency with Ω as the Earth's angular velocity. Here, $z = z(t)$ because of the mooring motion pull down. The solution for $A(z)$ is a simple exercise in least square analysis but not so for m. Therefore, multiple fits for a range of m values ($-0.5 < m < 0.5$ cpm) were generated, and the m's that gives the least residuals were chosen. Here, positive m means upward phase and downward energy propagation. A 48-h time and 20-m depth window were chosen for doing the fits, thus, giving time dependent estimates of the current amplitude and vertical wave number. Noise and tilting of the moorings results in some errors in the vertical wave number calculations, particularly for deep NIW currents at the DVLA where some values of m are negative. Table IV lists some statistics of the amplitude and vertical wave number fits for the six T-moorings. Figures 14 and 15 show example fits for two energetic NIW packets.

Figure 15 shows one of the most energetic NIW events observed, which lasted 5–10 days during mid-winter ice conditions. The currents reach a peak of 20 cm/s and are relatively uniform in depth. The rotary spectra confirm the anticyclonic circulation of the waves. The geographic and temporal variability of the NIWs are shown in Fig. 16, including NIW estimates from the deep observations from the DVLA. As previously mentioned, the deep NIW currents observed on the DVLA are quite weak in comparison to the upper ocean currents (Worcester *et al.*, 2018).

Figure 16 shows that, in general, NIW energy is larger when there is no ice cover, but there are some significant events in the presence of ice, including the largest events in the record around yearday 370 at the T-moorings. They are

TABLE IV. Statistics of the fits for the T-moorings.

	T1	T2	T3	T4	T5	T6
Date	2–5 October	4–8 October	1–7 January	23 June-12 July	21–25 October	23–29 June
Mean amplitude (cm/s)[a]	8.38	10.29	14.01	7.49	12.24	7.22
RMS amplitude (cm/s)	2.61	2.21	4.71	3.12	5.33	2.11
Vertical wave number (cycles per minute, cpm)	0.041	0.003	0.092	0.013	0.059	0.05
RMS vertical wave number (cpm)	0.018	0.001	0.054	0.009	0.037	0.028

[a]The error covariance was assumed diagonal with a constant value of 5 cm/s, estimated from the current variability when NIWs were absent.

not observed at the DVLA as the measurements were made deeper in the water column. There is not much coherence between the NIW signals across the array except for the aforementioned large event.

V. SUMMARY AND CONCLUSIONS

In this work, the thermohaline and current structures of the Beaufort Sea are studied from the yearlong moored CANAPE data and ship CTD observations (e.g., Fig. 2). Water masses of ASW, PSW, PWW, and AW were characterized by temperature and salinity properties, and two haloclines were observed. This environment creates two well-known sound channels, a strong surface duct extending to a 75.8–104.7-m depth and a weaker Beaufort duct below the surface duct extending to a 208.4–255.2-m depth. The sound speed variability was quantified in the deeper section of the surface duct and through and below the Beaufort duct. In this upper ocean region, internal wave vertical displacements are seen to be small (Fig. 11) and the resulting sound speed perturbations are correspondingly small especially through the axis of the Beaufort duct where the sound speed gradient is small (Fig. 13). The largest observed sound speed variability is in the 50–100 m-depth range and is due to spice (Fig. 13). It is expected that this strong variability would extend all the way to the sea surface. This variability implies that surface duct acoustic propagation will experience scattering not only from the sea surface but also from the water column. In addition, the upper ocean variability determines the upper bound on the Beaufort duct, modifying

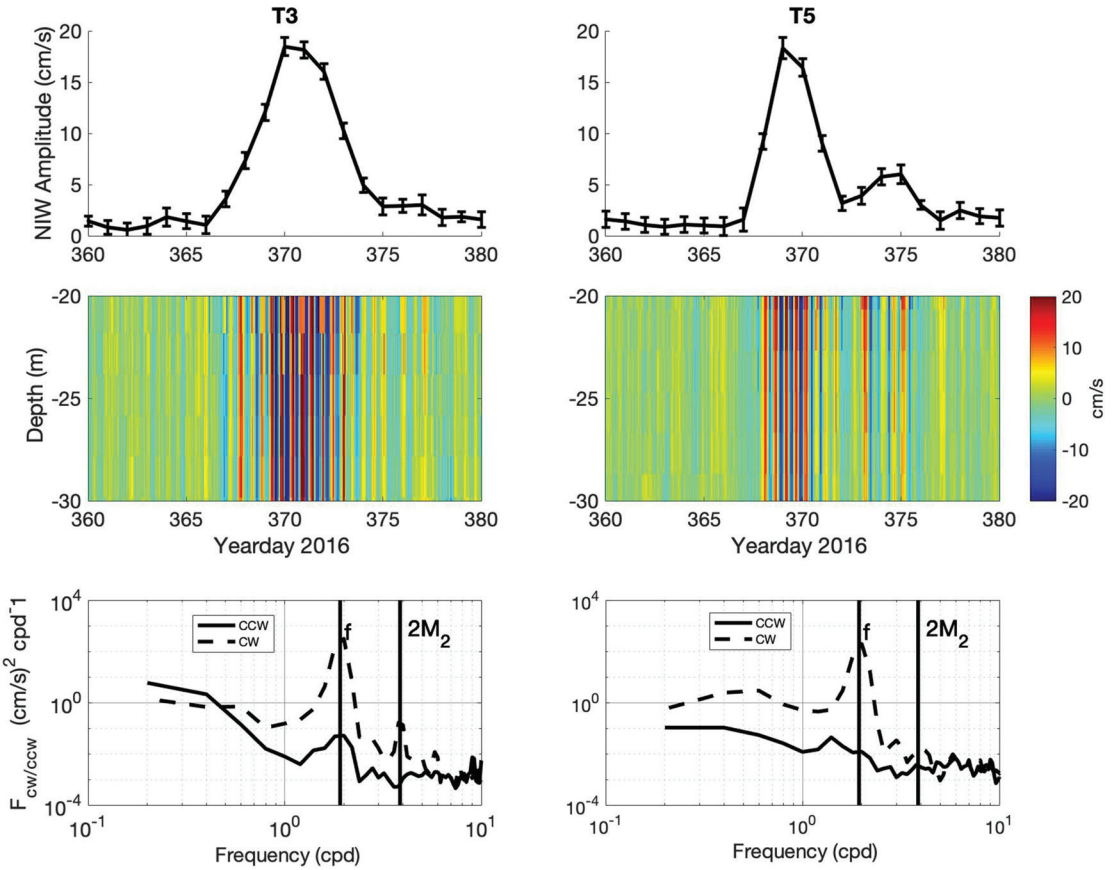

FIG. 15. Depth-averaged NIW amplitudes with error bars (upper), observed NIW packets (middle), and rotary spectra (lower). Clockwise (CW) rotation is plotted as a dashed line, and counterclockwise (CCW) rotation is plotted as a solid line. Mooring T3 is on the left, T5 is on the right, and the time interval is between 25 December 2016 (yearday 360) and 14 January 2017 (yearday 380).

https://doi.org/10.1121/10.0003601

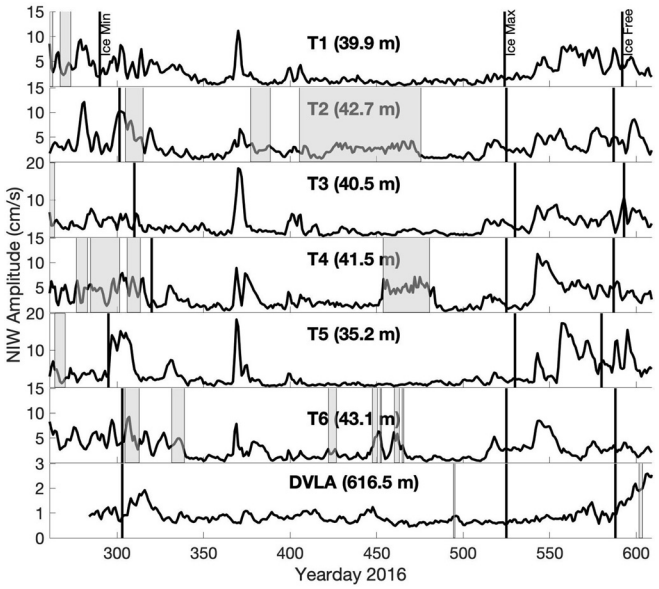

FIG. 16. Depth-averaged NIW amplitudes at the T-moorings and DVLA between 16 September 2016 (yearday 260) and 31 August 2017 (yearday 609). Gray regions indicate the mooring pull-down events that are bigger than 30 m. Vertical lines show the ice minimum, ice maximum, and ice-free periods, estimated from 11 to 12 kHz acoustic scattering measurements off the ocean surface. Each title is labeled with the approximate depth of the ADCP.

mode trapping (Fig. 5). Specific acoustic effects occurring here will be the focus of future work analyzing the long range transmission data. While the observations have quantified the depth and time scales of sound speed variability, an important open question concerns the horizontal scales and possible inhomogeneity and anisotropy.

In summary, significant fluctuations were observed from eddies, and smaller changes were seen within the super-inertial or internal wave band. Displacement spectra were used to quantify this variability, and the shapes and energy levels of the spectra are seen to vary with the depth and season (Fig. 10). For example, an enhanced eddy field was observed during the spring and summer. In addition, the super-inertial spectra vary significantly over the season and depth and do not agree with the GM spectral shape. On the other hand, a strong peak at tidal/inertial frequency and a moderate peak at twice the tidal frequency existed in all depths and seasons. In the upper 100 m, the frequency spectra of displacement had a rather flat spectral slope in the frequency range of 2–30 cpd with values of -0.8 to -1 (Fig. 10). In comparison the spicy sound speed spectra shows power law slopes of of -1.5 to -1.7 (Fig. 12). Regarding the RMS displacement in the super-inertial band, it is found to be consistent with the WKB approximation using a reference level of $\zeta_0 = 1.5$ m, which is approximately 20% of the GM level (Fig. 11). The sub-inertial RMS displacements were responsible for nearly 80% of the total variance, indicating the dominance of eddies.

Finally, the current amplitudes and vertical wave numbers were fit by a NIW model. Larger amplitudes appeared mainly under the ice-free surface, and the majority of them were downward propagating waves with anticyclonic circulation. A striking feature of the NIW amplitude is that a big wave packet was observed at nearly all of the moorings roughly between yeardays 360 and 380 under the surface of thin ice. These wave packets caused significant variations in the horizontal current in the upper ocean but did not seem to penetrate into the deeper ocean ($\sim$500 m) where there were other ADCP observations at the DVLA. It remains to be demonstrated that these strong inertial currents (up to 20 cm/s) are acoustically significant, although spectra of the observed travel times show an inertial peak (Worcester *et al.*, 2018).

In this work, sound speed and current variability from eddies, internal waves, spice, and NIWs have been quantified with the aim to use this information in the interpretation and modeling of the long range low frequency transmissions made across the CANAPE array. Specifically, the impact of these structures on normal mode propagation in the surface duct and Beaufort duct will be investigated and analyses will be carried out to study the variability of ray-like time front arrivals.

ACKNOWLEDGMENTS

This research was supported by the Office of Naval Research (ONR) and M.K. was supported by an ONR Ocean Acoustics Graduate Student Fellowship under Award No. N00014-19-1-2203. The 600 kHz ADCP and IPS ice draft data were supported by the ONR Arctic and Global Prediction Program (ONR 322AG) under Award No. N00014-15-1-2782. This material is based on work supported by the ONR under Award No. N00014-15-2068. Any opinions, findings, and conclusions or recommendations expressed in this publication are those of the authors and do not necessarily reflect the views of the ONR.

APPENDIX: DERIVATION OF THE TRAPPING RULE FOR A TWO TURNING POINT DUCT

Assume there is a symmetric bilinear duct with sound speed gradient γ. The duct has axial sound speed c_a and a vertical extent δz between two turning points z^- and z^+. The sound speed at the turning points is $c_m = c_a + \gamma\delta z/2$. The two turning point quantization condition (Colosi, 2016) for a symmetric profile is used to get the cutoff or minimum frequency, $\omega_{\min}$, (Urick, 1975) and is given by

$$2\omega_{\min}\int_{z_a}^{z^-}\sqrt{\frac{1}{c^2(z)}-\frac{1}{c_m^2}}dz = \pi(n-1/2). \tag{A1}$$

Using $c(z) = c_a + \gamma(z - z_a)$, the definition of c_m, and the fact that the gradient is weak, Eq. (1) can be approximated by

$$\frac{2\omega_{\min}}{c_m}\int_{z_a}^{z^-}\sqrt{\frac{\gamma\delta z}{c_a}-\frac{2\gamma(z-z_a)}{c_a}}dz = \pi(n-1/2). \tag{A2}$$

The integral can be solved, yielding

$$\omega_{\min} = \left(\frac{c_a^3}{2\gamma}\right)^{1/2} \left(\frac{2}{\delta z}\right)^{3/2} \frac{3\pi}{4}(n - 1/2), \tag{A3}$$

where $c_m \simeq c_a$ is used. Writing $\gamma = 2\delta c/\delta z$, it can further be written as

$$\omega_{\min} = \left(\frac{c_a^3}{\delta c}\right)^{1/2} \frac{1}{\delta z}\frac{3\pi}{2\sqrt{2}}(n - 1/2), \tag{A4}$$

where $f_{\min}(\text{Hz}) = \omega_{\min}/2\pi$.

Becker, J., Sandwell, D., Smith, W., Braud, J., Binder, B., Depner, J., Fabre, D., Factor, J., Ingalls, S., Kim, S., Ladner, R., Marks, K., Nelson, S., Pharaoh, A., Trimmer, R., Von Rosenberg, J., Wallace, G., and Weatherall, P. (**2009**). "Global bathymetry and elevation data at 30 arc seconds resolution: SRTM30_PLUS," Mar. Geodesy **32**(4), 355–371.

Bell, T., Jr. (**1975**). "Topographically generated internal waves in the open ocean," J. Geophys. Res. **80**(3), 320–327.

Brannigan, L., Johnson, H., Lique, C., Nycander, J., and Nilsson, J. (**2017**). "Generation of subsurface anticyclones at arctic surface fronts due to a surface stress," J. Phys. Oceanogr. **47**(11), 2653–2671.

Carpenter, J., and Timmermans, M.-L. (**2012**). "Deep mesoscale eddies in the Canada basin, Arctic ocean," Geophys. Res. Lett. **39**(20), L20602.

Colosi, J. A. (**2016**). *Sound Propagation Through the Stochastic Ocean* (Cambridge University Press, Cambridge, UK).

Colosi, J. A., Duda, T. F., Lin, Y.-T., Lynch, J. F., Newhall, A. E., and Cornuelle, B. D. (**2012**). "Observations of sound-speed fluctuations on the New Jersey continental shelf in the summer of 2006," J. Acoust. Soc. Am. **131**(2), 1733–1748.

Colosi, J. A., Kucukosmanoglu, M., Worcester, P. F., Dzieciuch, M., Proshutinsky, A. Y., Krishfield, R. A., and Nash, J. D. (**2018**). "An overview of Beaufort Sea eddies, internal waves, and spice from several recent field efforts and implications for acoustic propagation," J. Acoust. Soc. Am. **144**(3), 1665.

Colosi, J. A., Van Uffelen, L. J., Cornuelle, B. D., Dzieciuch, M. A., Worcester, P. F., Dushaw, B. D., and Ramp, S. R. (**2013**). "Observations of sound-speed fluctuations in the western Philippine Sea in the spring of 2009," J. Acoust. Soc. Am. **134**(4), 3185–3200.

D'Asaro, E. A. (**1985**). "The energy flux from the wind to near-inertial motions in the surface mixed layer," J. Phys. Oceanogr. **15**(8), 1043–1059.

DiMaggio, D., Colosi, J. A., Joseph, J., Pearson, A., Worcester, P. F., and Dzieciuch, M. A. (**2018**). "Observations of thermohaline sound-speed structure induced by internal waves and spice in the summer 2015 Canada Basin marginal ice zone," Elem. Sci. Anthropocene **6**(1), 30.

Dosser, H. V., and Rainville, L. (**2016**). "Dynamics of the changing near-inertial internal wave field in the Arctic Ocean," J. Phys. Oceanogr. **46**(2), 395–415.

Dosser, H. V., Rainville, L., and Toole, J. M. (**2014**). "Near-inertial internal wave field in the Canada Basin from ice-tethered profilers," J. Phys. Oceanogr. **44**(2), 413–426.

Duda, T. F., Collis, J. M., Lin, Y.-T., Newhall, A. E., Lynch, J. F., and DeFerrari, H. A. (**2012**). "Horizontal coherence of low-frequency fixed-path sound in a continental shelf region with internal-wave activity," J. Acoust. Soc. Am. **131**(2), 1782–1797.

Dzieciuch, M., Munk, W., and Rudnick, D. L. (**2004**). "Propagation of sound through a spicy ocean, the SOFAR overture," J. Acoust. Soc. Am. **116**(3), 1447–1462.

Fine, E. C., MacKinnon, J. A., Alford, M. H., and Mickett, J. B. (**2018**). "Microstructure observations of turbulent heat fluxes in a warm-core Canada Basin eddy," J. Phys. Oceanogr. **48**(10), 2397–2418.

Flatté, S., Dashen, R., Munk, W., Watson, K., and Zachariasen, F. (**1979**). *Sound Transmission through a Fluctuating Ocean*, edited by S. M. Flatte (Cambridge University Press, Cambridge, UK).

Garrett, C., and Kunze, E. (**2007**). "Internal tide generation in the deep ocean," Annu. Rev. Fluid Mech. **39**, 57–87.

Haine, T. W., Curry, B., Gerdes, R., Hansen, E., Karcher, M., Lee, C., Rudels, B., Spreen, G., de Steur, L., Stewart, K. D., and Woodgate, R. (**2015**). "Arctic freshwater export: Status, mechanisms, and prospects," Global Planet. Change **125**, 13–35.

Halle, C., and Pinkel, R. (**2003**). "Internal wave variability in the Beaufort Sea during the winter of 1993/1994," J. Geophys. Res.: Oceans **108**(C7), 3210.

Hebert, D., and Moum, J. (**1994**). "Decay of a near-inertial wave," J. Phys. Oceanogr. **24**(11), 2334–2351.

Levine, M. D., Paulson, C. A., and Morison, J. H. (**1987**). "Observations of internal gravity waves under the Arctic pack ice," J. Geophys. Res.: Oceans **92**(C1), 779–782.

Lyard, F. H. (**1997**). "The tides in the Arctic Ocean from a finite element model," J. Geophys. Res.: Oceans **102**(C7), 15611–15638.

Martini, K. I., Simmons, H. L., Stoudt, C. A., and Hutchings, J. K. (**2014**). "Near-inertial internal waves and sea ice in the Beaufort Sea," J. Phys. Oceanogr. **44**(8), 2212–2234.

Maslanik, J., Fowler, C., Stroeve, J., Drobot, S., Zwally, J., Yi, D., and Emery, W. (**2007**). "A younger, thinner arctic ice cover: Increased potential for rapid, extensive sea-ice loss," Geophys. Res. Lett. **34**(24), L24501.

McPhee, M. (**2008**). *Air-Ice-Ocean Interaction: Turbulent Ocean Boundary Layer Exchange Processes* (Springer Science and Business Media, Springer, New York).

Morison, J. H., Long, C. E., and Levine, M. D. (**1985**). "Internal wave dissipation under sea ice," J. Geophys. Res.: Oceans **90**(C6), 11959–11966.

Munk, W. (**1981**). "Internal waves and small-scale processes," in *Evolution of Physical Oceanography* (The MIT Press, Cambridge, MA), pp. 264–291.

Munk, W., and Wunsch, C. (**1998**). "Abyssal recipes II: Energetics of tidal and wind mixing," Deep Sea Res., Part I **45**(12), 1977–2010.

Ostashev, V. E., and Wilson, D. K. (**2015**). *Acoustics in Moving Inhomogeneous Media* (CRC Press, Boca Raton, FL).

Overland, J. E. (**2009**). "Meteorology of the Beaufort Sea," J. Geophys. Res.: Oceans **114**(C1), C00A07.

Rainville, L., Lee, C. M., and Woodgate, R. A. (**2011**). "Impact of wind-driven mixing in the Arctic Ocean," Oceanography **24**(3), 136–145.

Rainville, L., and Woodgate, R. A. (**2009**). "Observations of internal wave generation in the seasonally ice-free Arctic," Geophys. Res. Lett. **36**(23), L23604.

Rigby, F. A. (**1976**). "Pressure ridge generated internal wave wakes at the base of the mixed layer in the Arctic Ocean," University of Washington.

Smith, W. H., and Sandwell, D. T. (**1997**). "Global sea floor topography from satellite altimetry and ship depth soundings," Science **277**(5334), 1956–1962.

Smith, W. H., and Sandwell, D. T. (**2014**). "Global topography," available at https://topex.ucsd.edu/www_html/mar_topo.html (Last viewed December 7, 2019).

Stroeve, J., Markus, T., Boisvert, L., Miller, J., and Barrett, A. (**2014**). "Changes in Arctic melt season and implications for sea ice loss," Geophys. Res. Lett. **41**(4), 1216–1225.

Stroeve, J. C., Kattsov, V., Barrett, A., Serreze, M., Pavlova, T., Holland, M., and Meier, W. N. (**2012**). "Trends in Arctic Sea ice extent from CMIP5, CMIP3 and observations," Geophys. Res. Lett. **39**(16), L16502.

Talley, L. D., Pickard, G. L., Emery, W. J., and Swift, J. H. (**2011**). *Descriptive Physical Oceanography: An Introduction* (Elsevier, Boston, MA).

Timmermans, M.-L., and Jayne, S. R. (**2016**). "The arctic ocean spices up," J. Phys. Oceanogr. **46**(4), 1277–1284.

Urick, R. J. (**1975**). *Principles of Underwater Sound* (McGraw-Hill, New York).

Worcester, P. F., Cornuelle, B. D., Dzieciuch, M. A., Munk, W. H., Howe, B. M., Mercer, J. A., Spindel, R. C., Colosi, J. A., Metzger, K., Birdsall, T. G., and Baggeroer, A. B. (**1999**). "A test of basin-scale acoustic thermometry using a large-aperture vertical array at 3250-km range in the eastern North Pacific Ocean," J. Acoust. Soc. Am. **105**(6), 3185–3201.

Worcester, P. F., Dzieciuch, M. A., Colosi, J. A., Proshutinsky, A. Y., Krishfield, R. A., Nash, J. D., and Kemp, J. N. (**2018**). "The 2016–2017 deep-water Canada basin acoustic propagation experiment (CANAPE): An overview," J. Acoust. Soc. Am. **144**(3), 1665.

Zhao, M., Timmermans, M.-L., Cole, S., Krishfield, R., Proshutinsky, A., and Toole, J. (**2014**). "Characterizing the eddy field in the Arctic Ocean halocline," J. Geophys. Res.: Oceans **119**(12), 8800–8817.